Supplementary Information

A Unique Morphology and Interface Dual-Engineering Strategy Enables the Holey C@VO_2 Cathode with Enhanced Storage Kinetics for Aqueous Zn-ion Batteries

Ming Yang[a,1], Dingtao Ma[a,b,1], Hongwei Mi[a,c], Xiaodan Yang[a], Yanyi Wang[a,*], Lingna Sun[a,c], Peixin Zhang[a,c,*]

[a] College of Chemistry and Environmental Engineering, Shenzhen University, Shenzhen, 518060, PR China

[b] Institute of Microscale Optoelectronics, Shenzhen University, Shenzhen, China, 518060

[c] Guangdong Flexible Wearable Energy and Tools Engineering Technology Research Centre Shenzhen University, Shenzhen, Guangdong, 518060, PR China

E-mail: pxzhang@szu.edu.cn

[1] These authors contribute equally to this work.

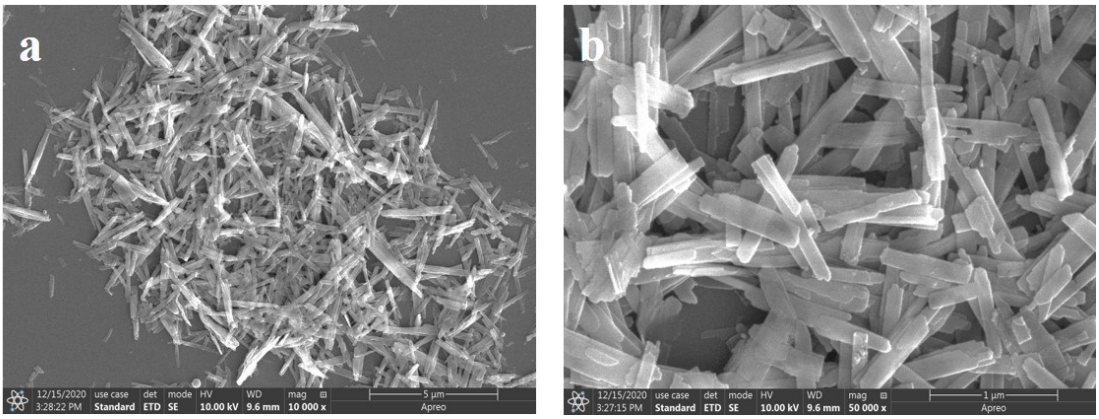

Figure S1. FESEM images of the VO_2 nanobelts at different magnification.

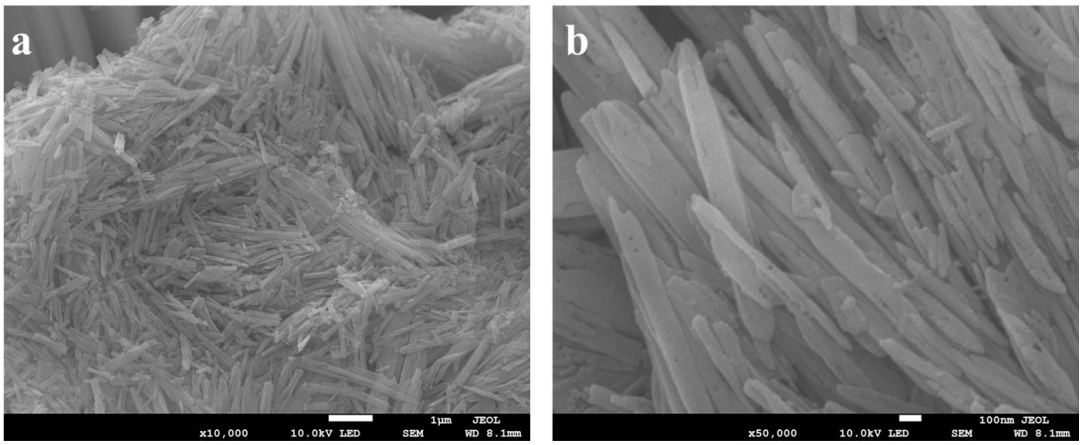

Figure S2. FESEM images of the holey VO_2 nanobelts at different magnification.

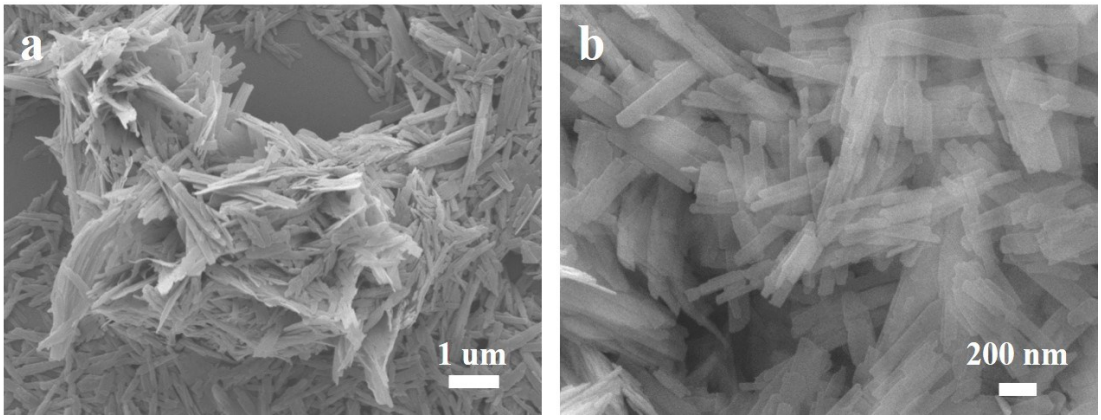

Figure S3. FESEM images of the C@VO_2 nanobelts at different magnification.

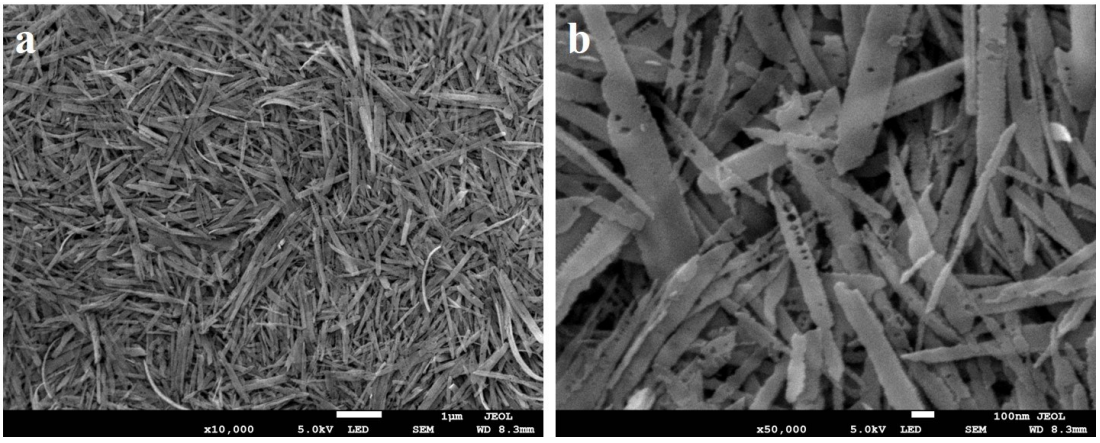

Figure S4. FESEM images of the holey C@VO_2 nanobelts at different magnification.

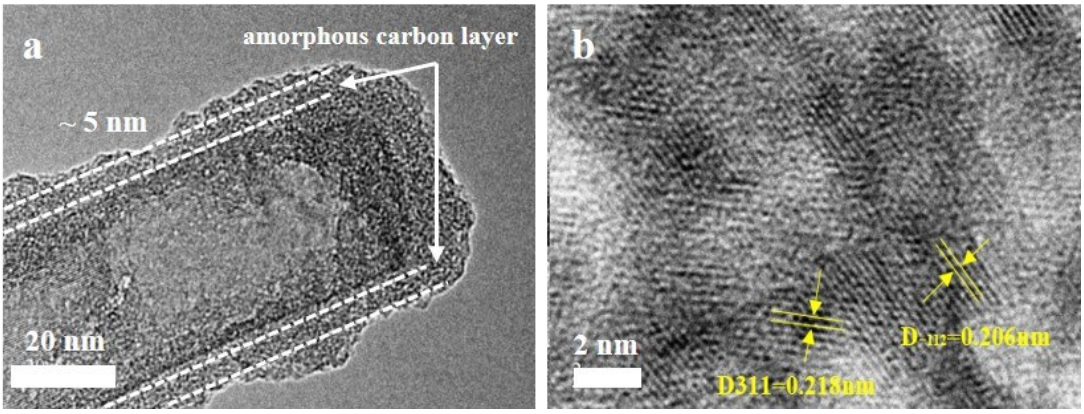

Figure S5. (a) TEM and (b) HRTEM images of the C@VO_2 nanobelts.

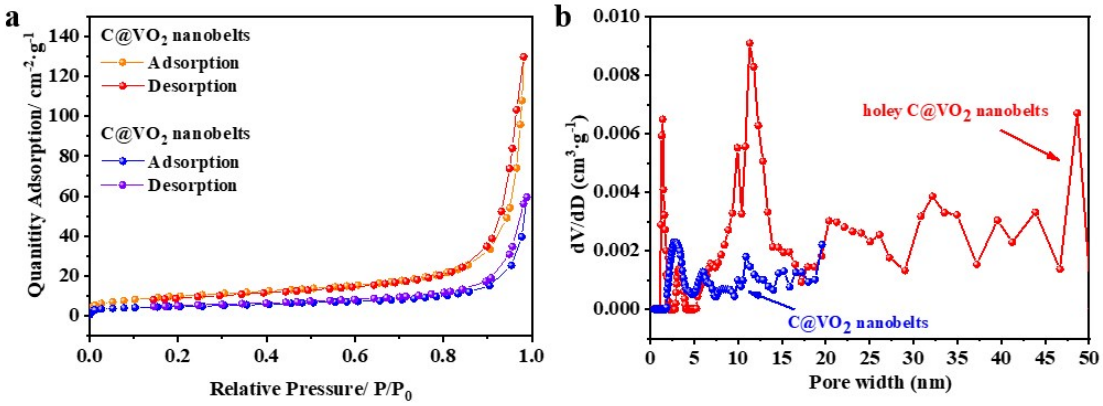

Figure S6. (a) N_2 adsorption/desorption isotherms and (b) corresponding pore size distribution of the holey C@VO_2 and C@VO_2 nanobelts.

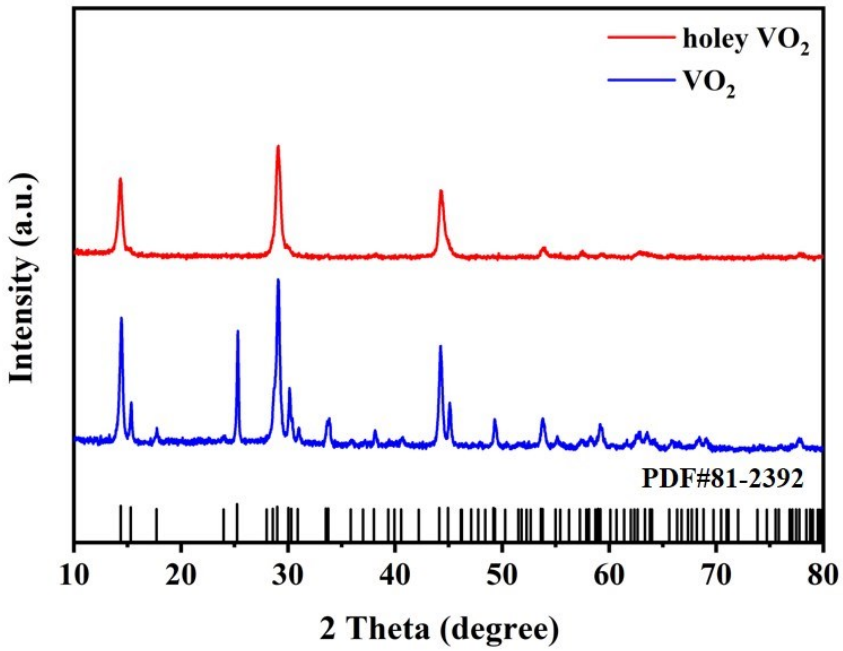

Figure S7. XRD pattern of the VO_2 and holey VO_2 nanobelts.

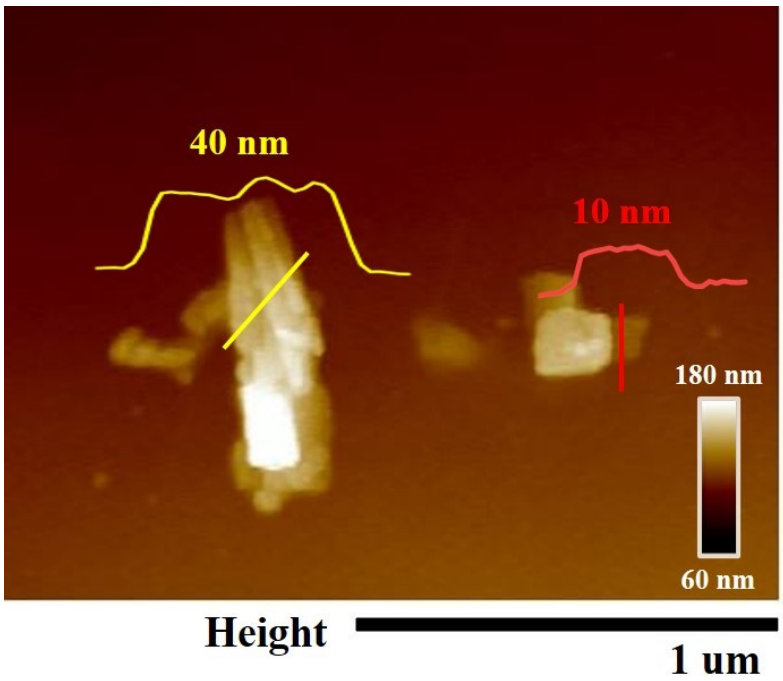

Figure S8. AFM image of the holey C@VO_2 nanobelts.

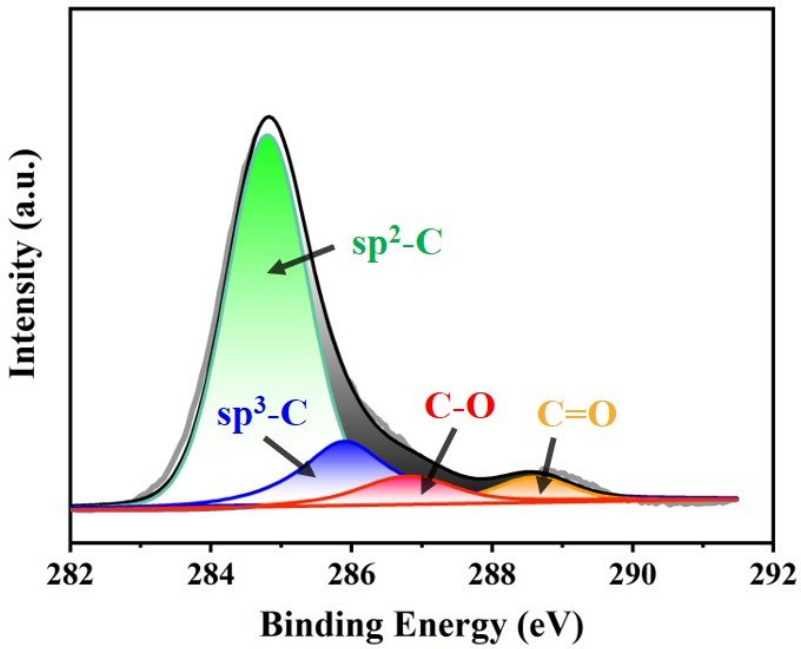

Figure S9. C 1s XPS spectrum of the holey C@VO_2 nanobelts.

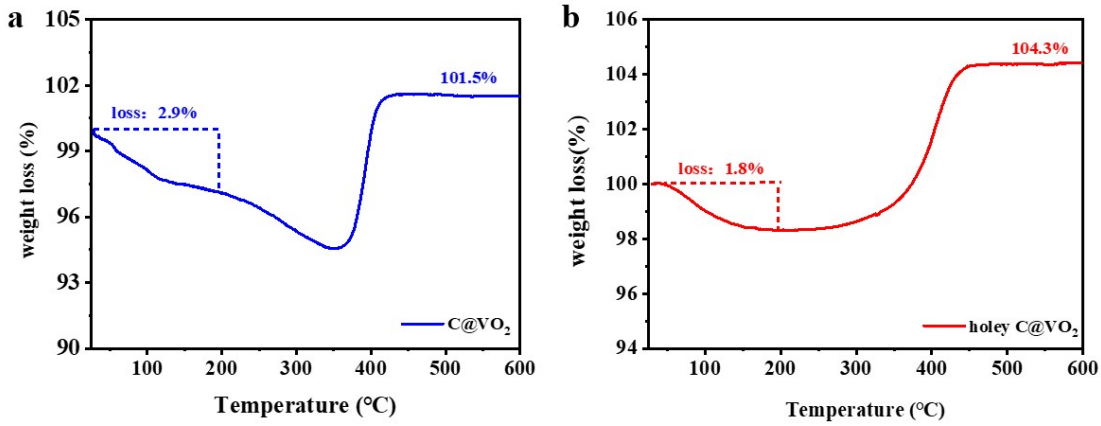

Figure S10. TGA curves of the C@VO_2, and holey C@VO_2 composites.

TGA analysis was employed to estimate the mass fraction of carbon in the C@VO_2 and holey C@VO_2 composites. Normally, the calcination of C@VO_2 and holey C@VO_2 composite in the air would cause the release of adsorbed H_2O molecules (G_{H2O}%) and carbon fraction (G_{carbon}%), as well as the oxidation of VO_2 to V_2O_5. Among them, the increment of mass fraction resulted from the oxidation of VO_2 can be theoretically calculated to be (1/2 ×181.88/82.94) × 100 wt% -1= 9.6 %. Therefore, the mass fraction of carbon can be approximately calculated according to the following

relationship：

G_{carbon} % = 109.6 % - G_{H2O}%- G_{act} %

As shown in Figure S10, there respectively exist a weight loss of about 2.9% and 1.8% before 200 °C for C@VO_2 and holey C@VO_2 composite, which should be ascribed to the release of adsorbed H_2O molecules. Then, the residual mass fraction (G_{act} *%)* of C@VO_2 and holey C@VO_2 composite are respectively about 101.5 wt% and 104.3 wt% when the calcination temperature was raised up to 600 ^oC. Therefore, the mass fraction of carbon in the C@VO_2 and holey C@VO_2 composite can be respectively calculated to be 5.2 wt% and 3.5 wt%.

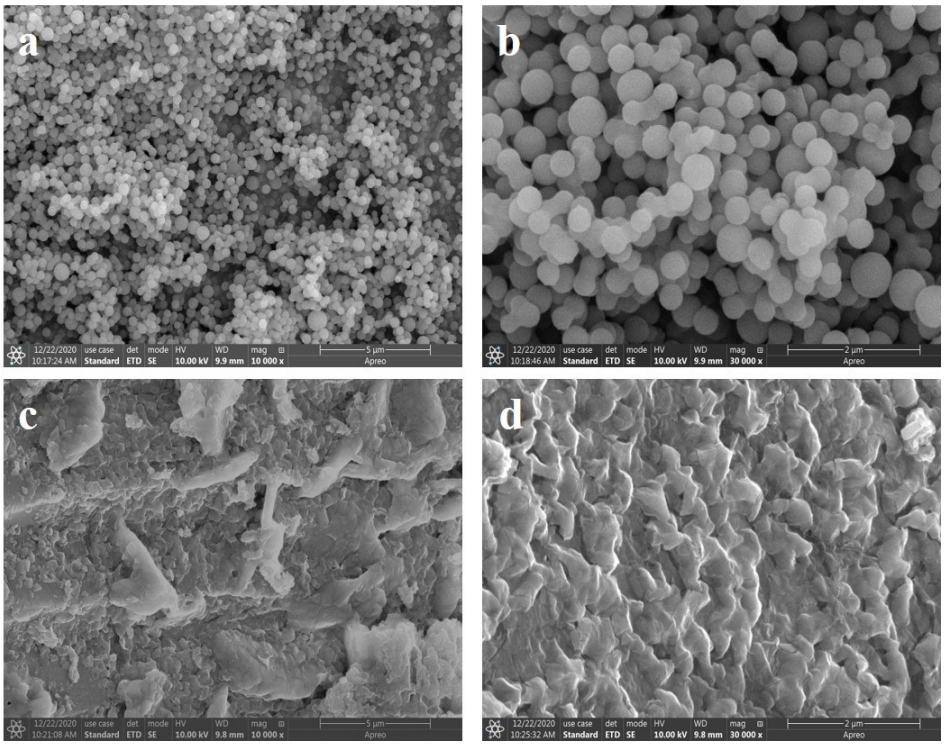

Figure S11. FESEM images of the carbon materials (a, b) derived from the glucose, and (c, d) after alkaline etching at different magnification.

As shown in Figure S11a and S11b, FESEM images indicate that the glucose-derived carbon material exhibits the relatively uniform sphere-like morphology. However, such carbon sphere material would turn into the carbon sheet material after alkaline etching treatment, as depicted in Figure S11c and S11d.

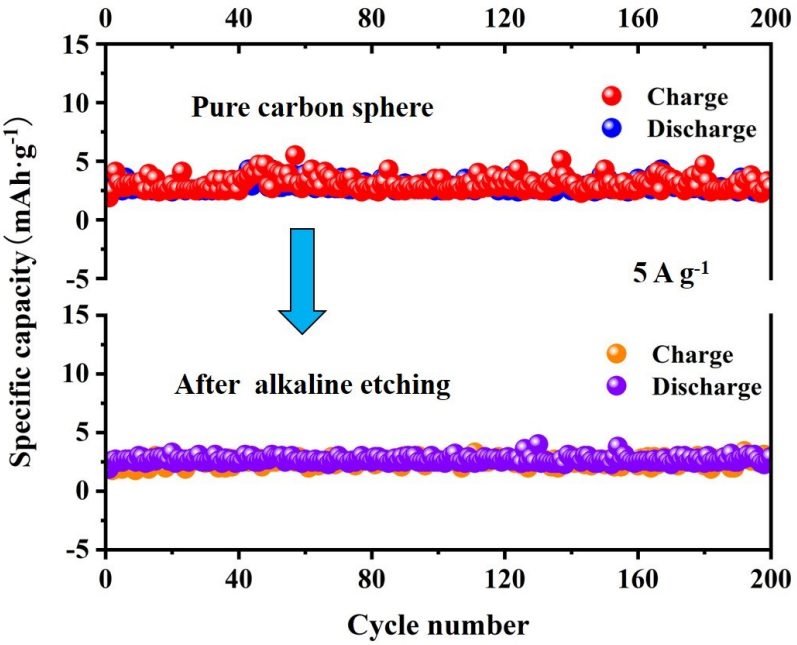

Figure S12. Cyclic performance of the glucose-derived carbon and alkaline etching carbon materials at 5 A g^{-1}.

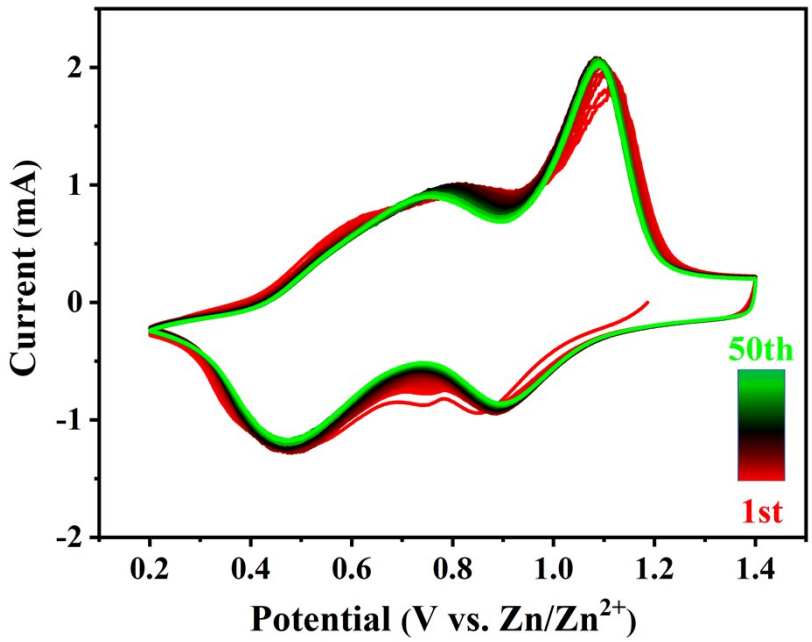

Figure S13. CV curves of the holey C@VO_2 cathode in the first fifty cycles at the scan rate of 1 mV s^{-1}.

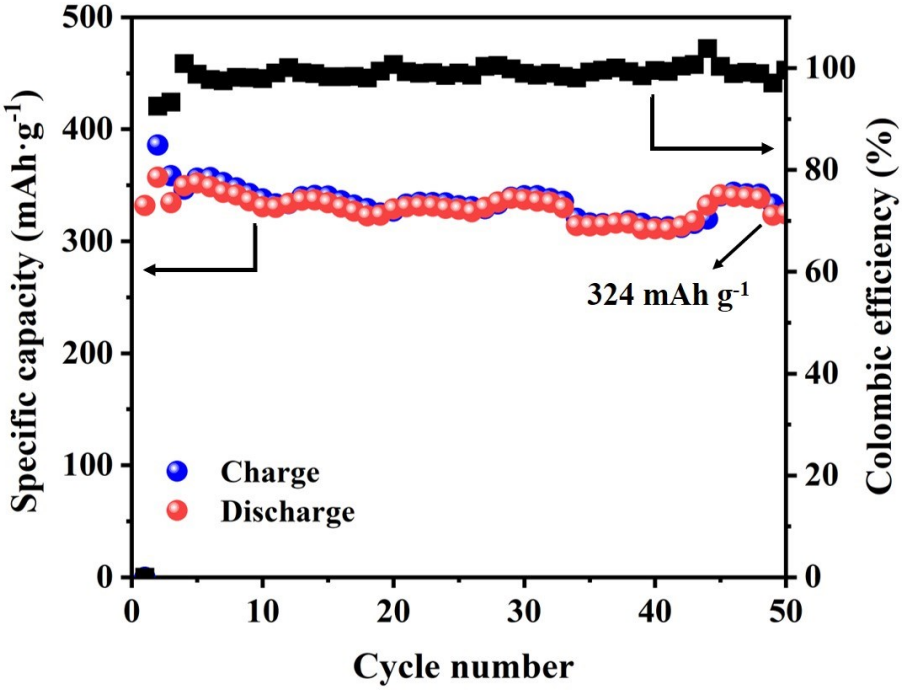

Figure S14. Cyclic performance of the holey VO_2 electrode at 0.2 A g^{-1} and the corresponding Coulombic efficiency.

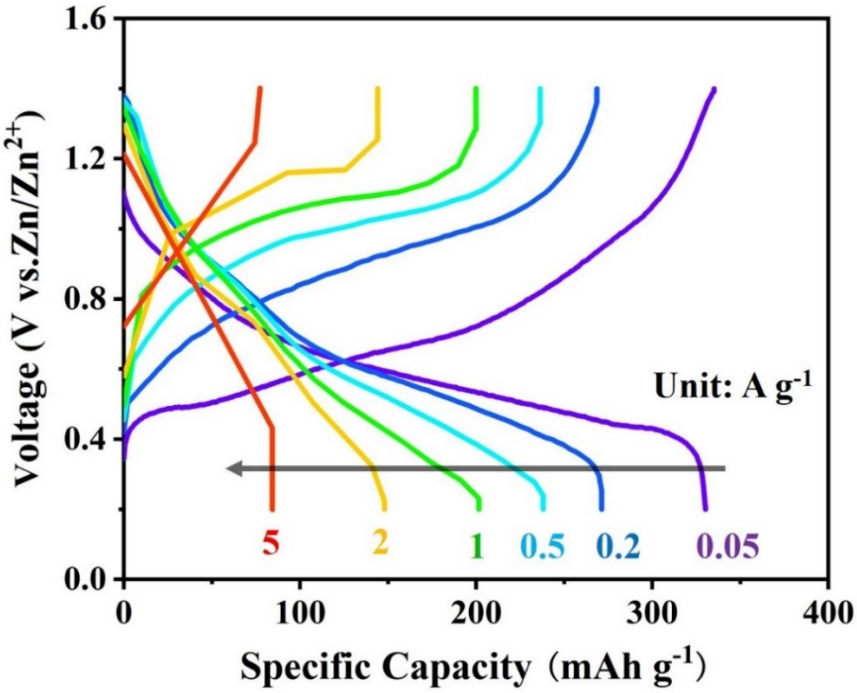

Figure S15. The charge-discharge curves of the C@VO_2 cathode under various current densities.

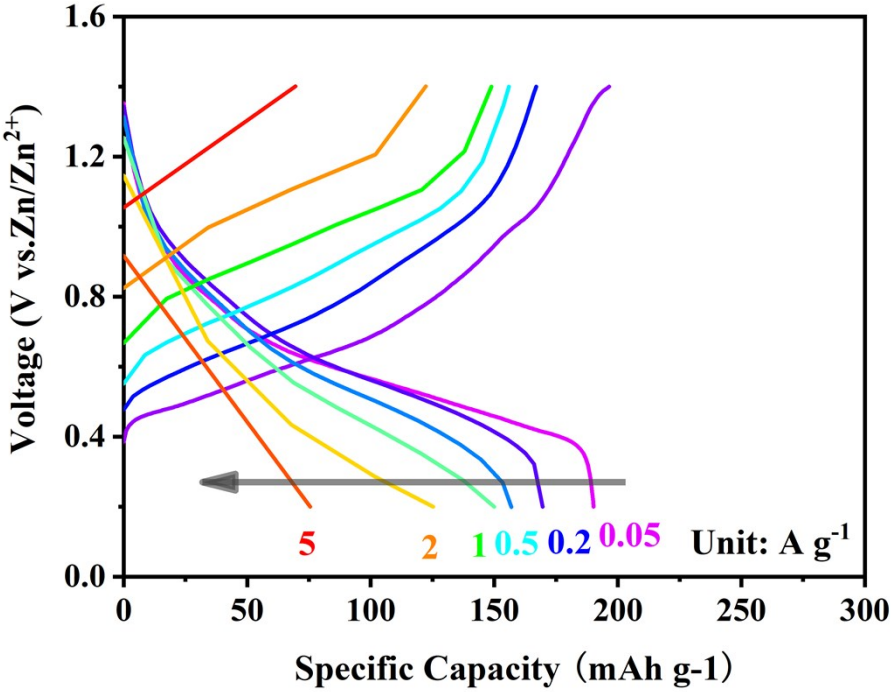

Figure S16. The charge-discharge curves of the VO_2 cathode under various current densities.

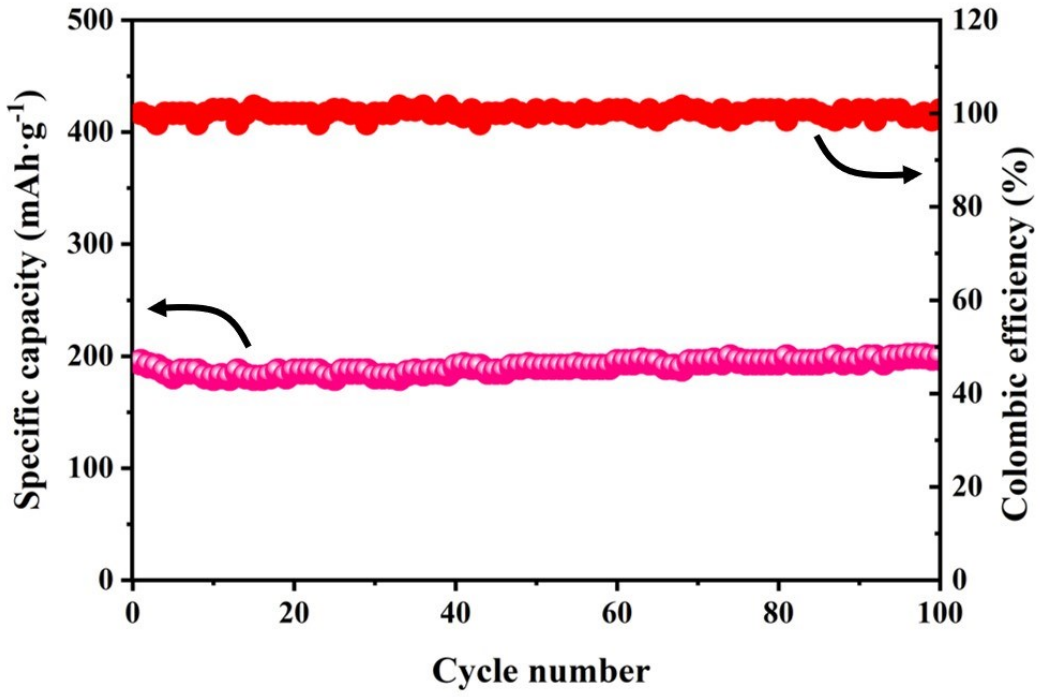

Figure S17. Cyclic performance of the C@VO_2 cathode at 5 A g^{-1} and the corresponding Coulombic efficiency.

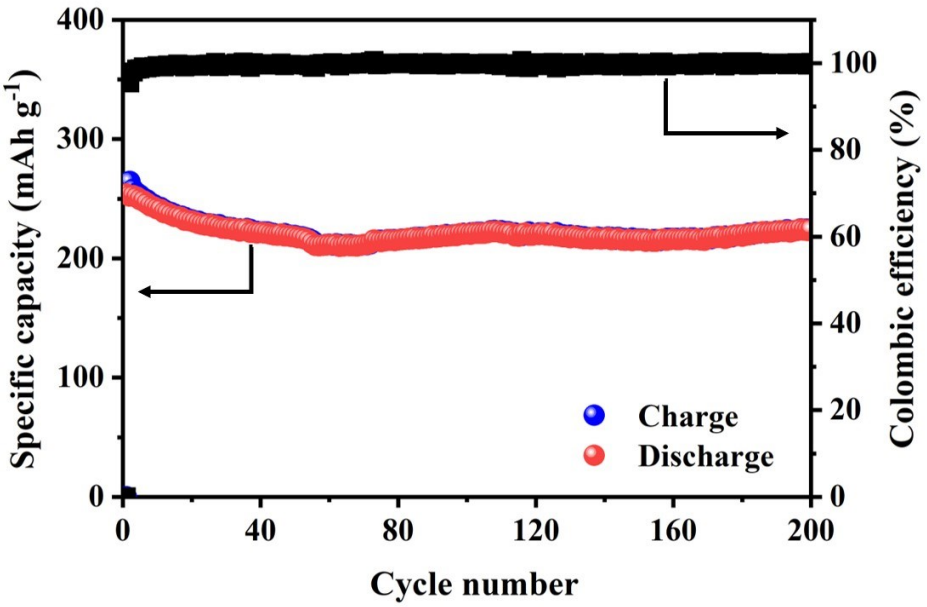

Figure S18. Cyclic performance of the holey VO_2 cathode at 5 A g^{-1} and the corresponding Coulombic efficiency.

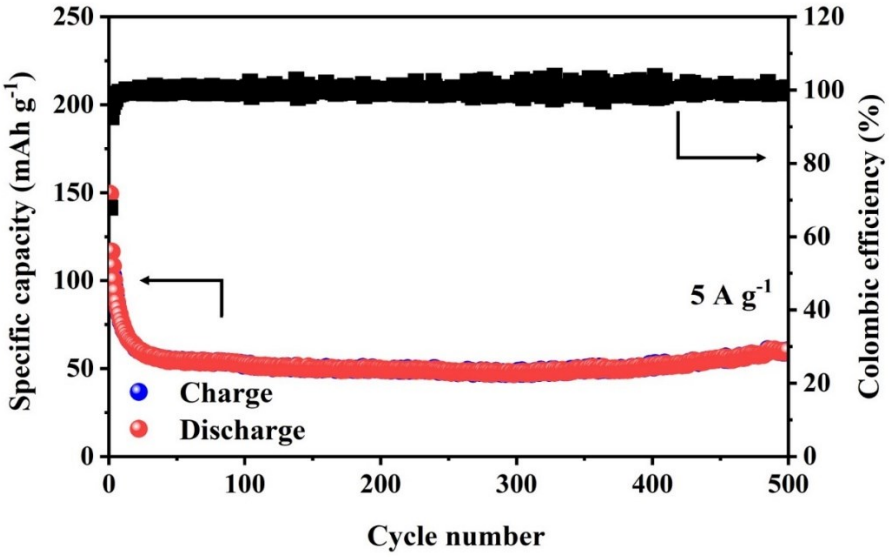

Figure S19. Cyclic performance of the VO_2 cathode at 5 A g^{-1} and the corresponding Coulombic efficiency.

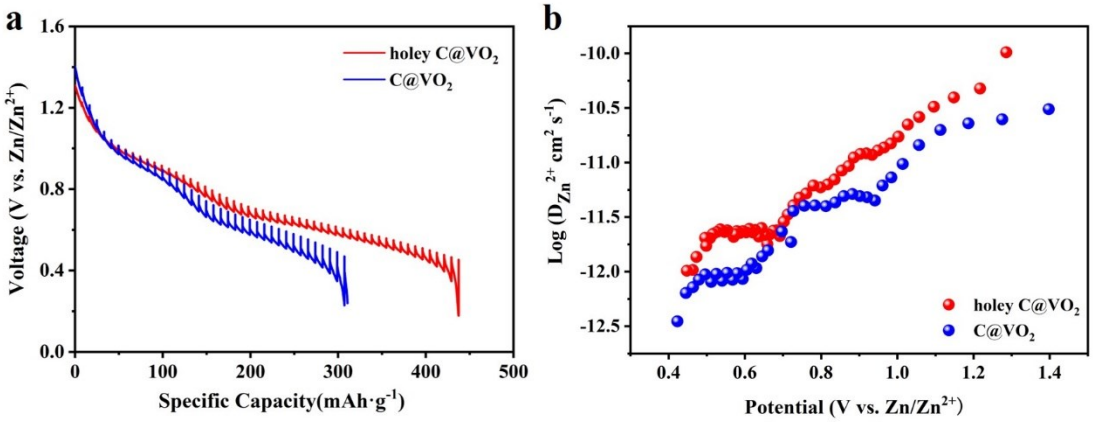

Figure S20. (a) GITT curves and (b) the corresponding Zn^{2+} diffusion coefficient of $C@VO_2$ and holey $C@VO_2$ electrode in the discharge process.

The Galvanostatic Intermittent Titration Technique (GITT) was used to further investigate the kinetics of Zn^{2+} solid-state diffusion of holey $C@VO_2$ and $C@VO_2$ during cycling. The GITT of discharge curves and corresponding diffusion coefficient of Zn^{2+} ($D_{Zn^{2+}}$) for holey $C@VO_2$ and $C@VO_2$ electrodes are respectively shown in Figure S20a and S20b. The results reveal that the $D_{Zn^{2+}}$ of holey $C@VO_2$ ranges from 1.3×10^{-12} to 1.2×10^{-10} cm^{-2} s^{-1} during the discharge process, which is higher than that of 3.13×10^{-13}~3.2×10^{-11} cm^{-2} s^{-1} for $C@VO_2$ electrode, demonstrating the holey sample a better storage kinetics for AZIBs.

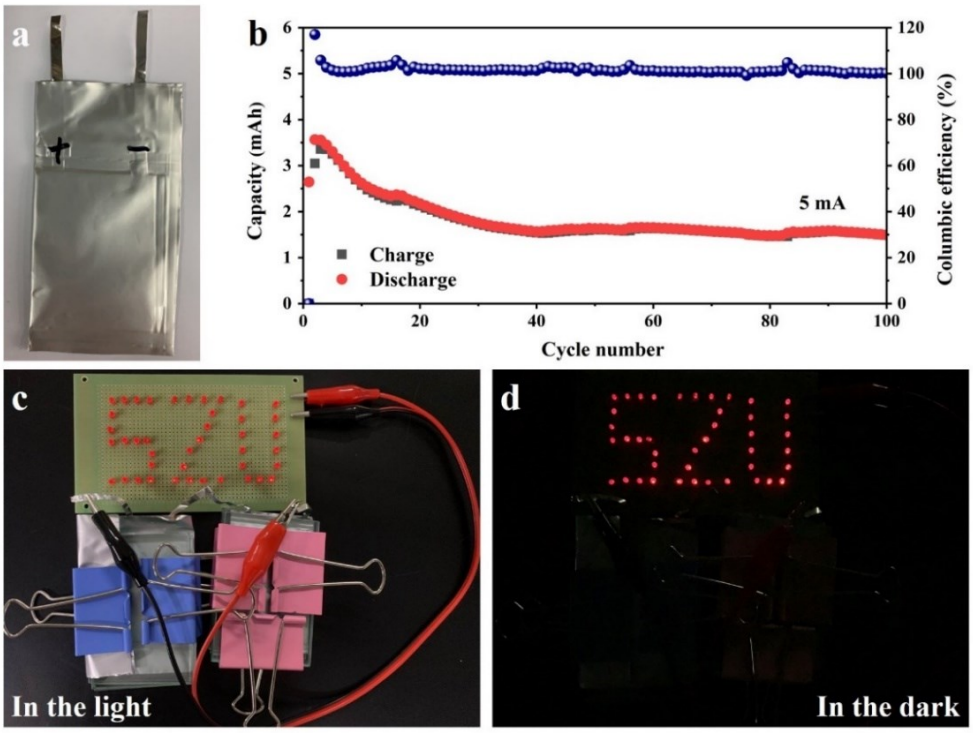

Figure S21. (a) Digital image of soft package battery constructed by the holey C@VO_2 cathode. (b) Cycle performance of soft package battery. (c, d) Two series batteries supply power for the pre-designed diode in the light and dark environments.

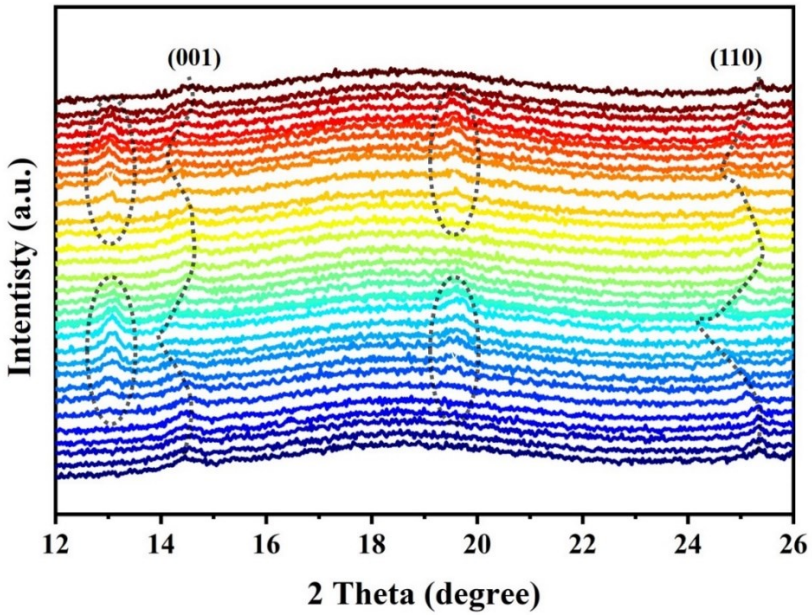

Figure S22 XRD patterns of the holey C@VO_2 electrode collected at different states during cycling between 12° and 26°.

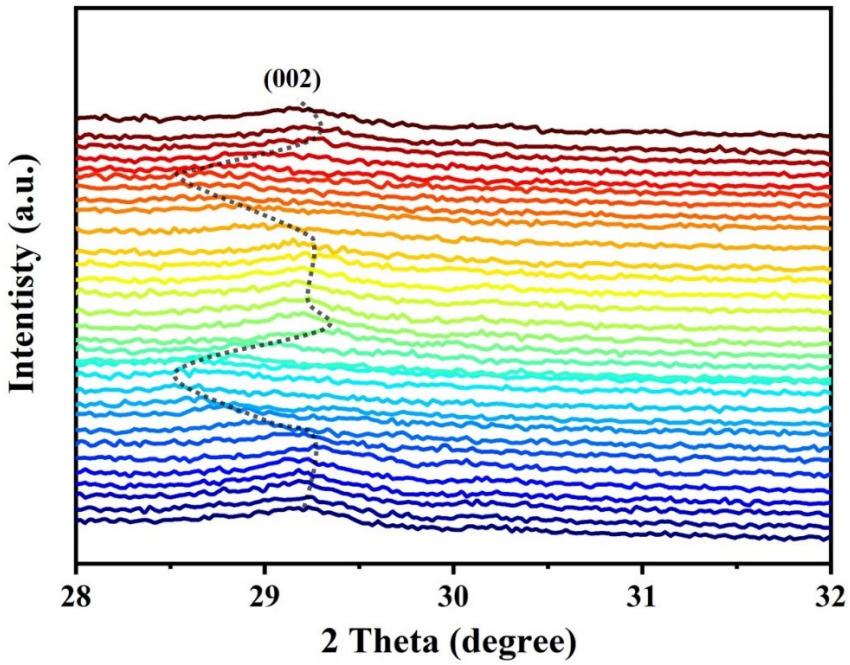

Figure S23. XRD patterns of the holey C@VO_2 electrode collected at different states during cycling between 28° and 32°.

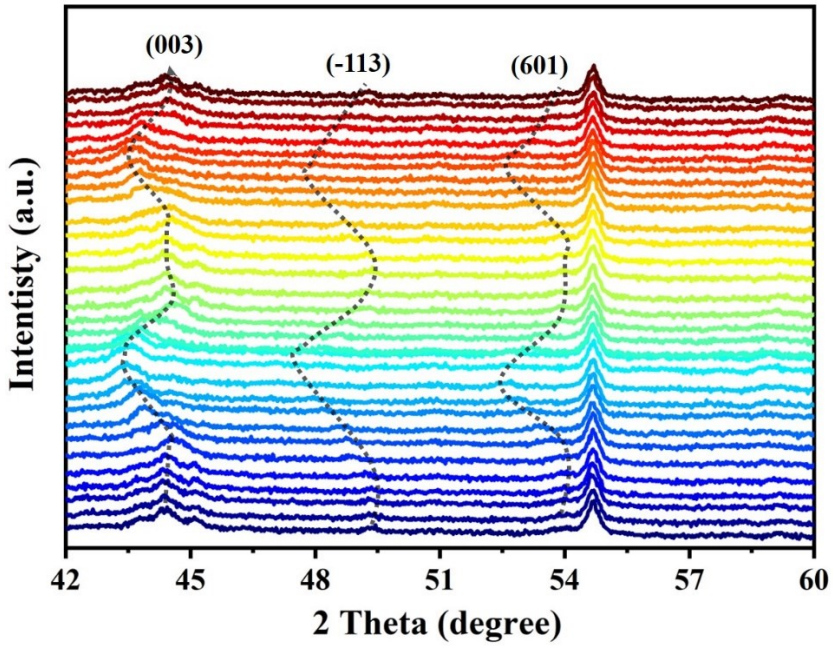

Figure S24. XRD patterns of the holey C@VO_2 electrode collected at different states during cycling between 42° and 60°.

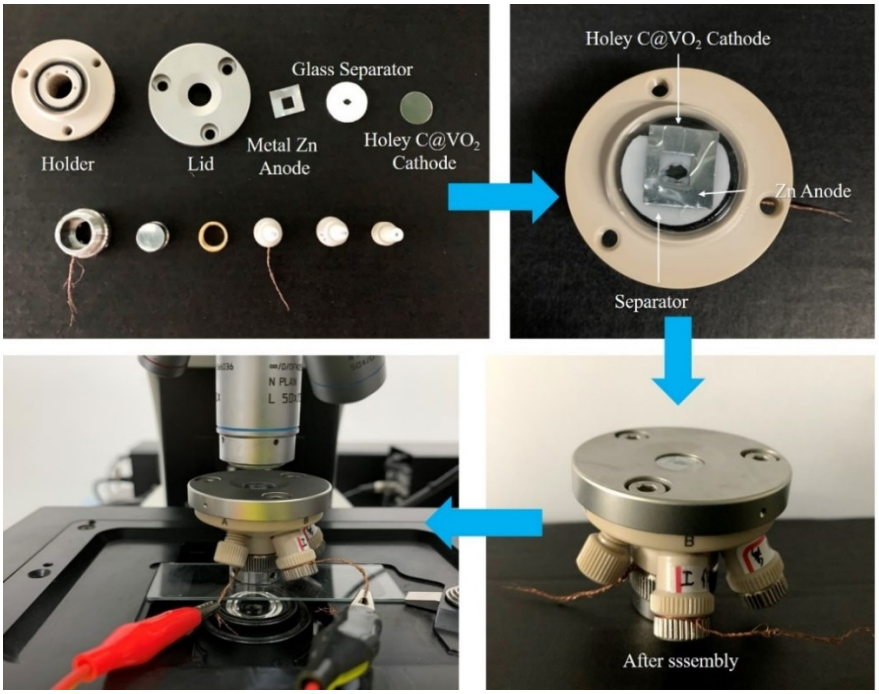

Figure S25. The assembly diagram of in-situ electrochemical Raman spectroscopy.

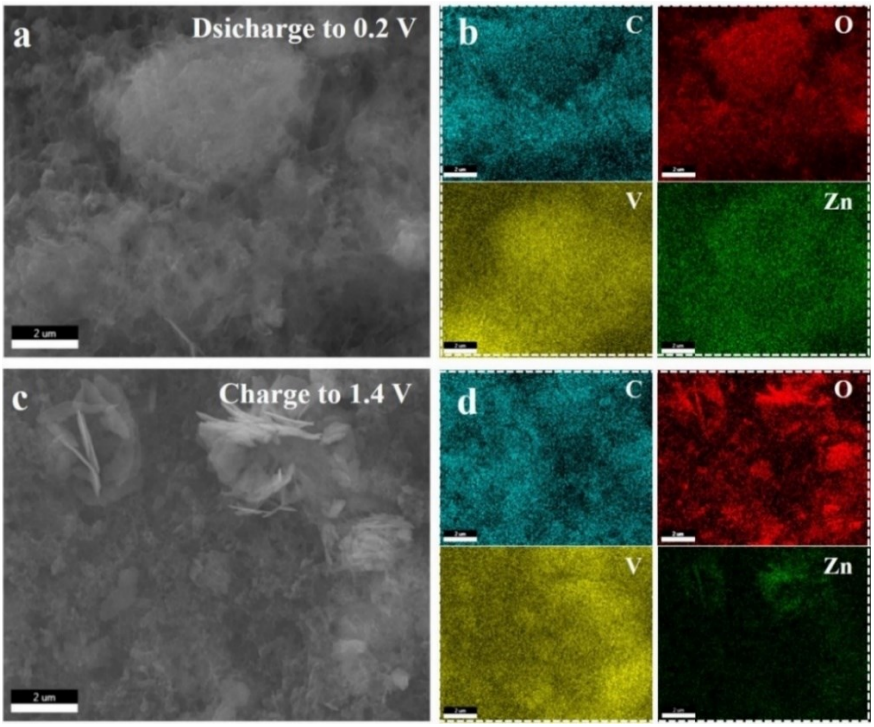

Figure S26. FESEM images and corresponding EDS mapping (C, O, V, and Zn elements) of the holey C@VO_2 electrode at the (a, b) fully discharged state and (c, d) fully charged state in the 15th cycle.

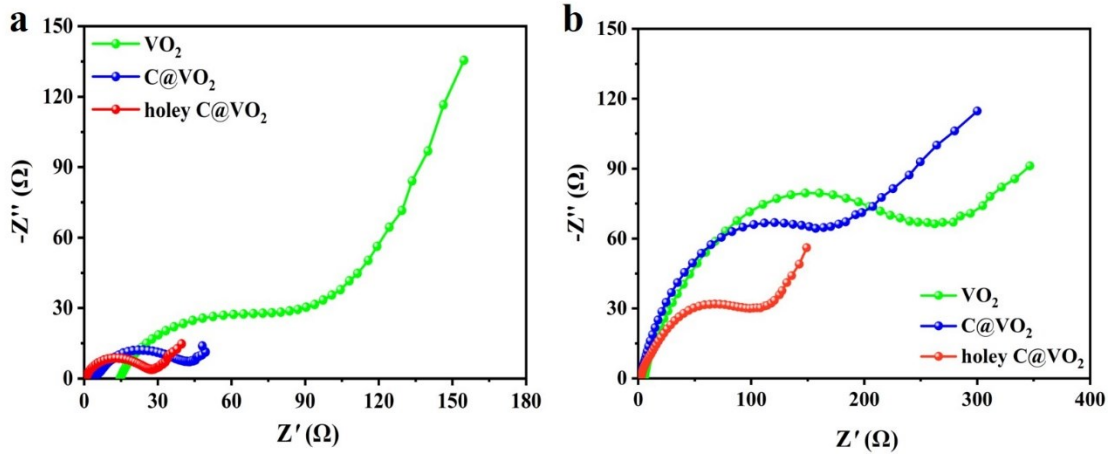

Figure S27. EIS spectra of the VO_2, C@VO_2, and holey C@VO_2 electrodes tested (a) before cycling, and (b) at fully charged state after 30th cycle.

To reveal the influence of carbon coating and alkaline etching on the transport kinetics of VO_2-based electrodes, EIS spectrum was employed to study the charge transfer impedance (R_{ct}) of VO_2, C@VO_2 and holey C@VO_2 electrodes. As shown in Figure 27a, the fitted results indicate that the pure VO_2 exhibits the largest R_{ct} of 53 Ω, while the carbon coating can effectively reduce the charge transfer impedance (35 Ω). More interestingly, the smallest R_{ct} of holey C@VO_2 (22.3 Ω) demonstrates that alkaline etching treatment can further boost the charge transfer among the cathode interface, which might be benefited from the unique holey architecture. Besides, Figure 27b shows that the holey C@VO_2 electrode can still performs the smallest R_{ct} (76 Ω) after 30 cycles, comparing with the value of 153 Ω and 205 Ω for the C@VO_2 and VO_2 electrodes, respectively. These results imply the excellent rate capability of holey C@VO_2 electrode, and be consistent with the electrochemical performance test discussed above.

Table S1 Summary of the comparison of electrochemical performance with other aqueous rechargeable Zn-ion batteries.

Materials	Electrolyte	Voltage window	Electrochemical performance	Ref.
Holey C@VO_2	3 M $Zn(CF_3SO_3)_2$	0.2-1.4V	332mAh g^{-1} (5 A g^{-1})	This work
V_2O_5	2 M $ZnSO_4$	0.2-1.6V	219 mAh g^{-1} (10 A g^{-1})	[1]
$Zn_{0.25}V_2O_5 \cdot nH_2O$	1 M $ZnSO_4$	0.5-1.4V	262 mAh g^{-1} (2.4 A g^{-1})	[2]
$NaCa_{0.6}V_6O_{16} \cdot 3H_2O$	3 M $Zn(CF_3SO_3)_2$	0.4-1.5V	231 mAh g^{-1} (2 A g^{-1})	[3]
$Ba_{1.2}V_6O_{16} \cdot 3H_2O$	2 M $ZnSO_4$	0.3-1.4V	130 mAh g^{-1} (5 A g^{-1})	[4]
$Mn_{0.15}V_2O_5 \cdot nH_2O$	1 M $Zn(ClO4)_2$	0.2-1.7V	153 mAh g^{-1} (10 A g^{-1})	[5]
$H_2V_3O_8$ Nanowire/Graphene	3 M $Zn(CF_3SO_3)_2$	0.2-1.6V	174 mAh g^{-1} (5 A g^{-1})	[6]
NW/graphene $H_2V_3O_8$				
V_6O_{13}	3 M $Zn(CF_3SO_3)_2$	0.2-1.5V	230 mAh g^{-1} (4 A g^{-1})	[7]
$V_3O_7 \cdot H_2O$	3 M $Zn(CF_3SO_3)_2$	0.1-1.7V	172 mAh g^{-1} (5 A g^{-1})	[8]
rGO-VS_2	1 M $ZnSO_4$	0.2-1.8V	187 mAh g^{-1} (5 A g^{-1})	[9]
VS_4@GO	1 M $Zn(CF_3SO_3)_2$	0.4-1.8V	180 mAh g^{-1} (1 A g^{-1})	[10]
VSe_2	2 M $ZnSO_4$	0.1-1.6V	146 mAh g^{-1} (2 A g^{-1})	[11]
$CoFe(CN)_6$	4 M $Zn(CF_3SO_3)_2$	0.7-2V	109 mAh g^{-1} (3 A g^{-1})	[12]
PA-COF	1 M $ZnSO_4$	0.2-16V	153 mAh g^{-1} (1 A g^{-1})	[13]
Bi_2S_3-PEDOT	1 M $Zn(CF_3SO_3)_2$ + 21 M LiTFSI	0-2.5V	131mAh g^{-1} (2 A g^{-1})	[14]
Rich-Co_3O_4	2 M $ZnSO_4$ + 0.2 M $CoSO_4$	0.8-2.2V	158 mAh g^{-1} (1 A g^{-1})	[15]
Mn_3O_4	2 M $ZnSO_4$	0.2-1.85V	125 mAh g^{-1} (5 A g^{-1})	[16]
O-MnO_2	2 M $ZnSO_4$ + 0.2	1.0-1.8V	120 mAh g^{-1} (5 A g^{-1})	[17]

	M $MnSO_4$			
A-$MnO_{2-\delta}$	2 M $ZnSO_4$ + 0.2 M $MnSO_4$	1.0-1.9V	147 mAh g^{-1} (1 A g^{-1})	[18]
MnO	2 M $ZnSO_4$ + 0.2 M $MnSO_4$	0.9-1.8V	115 mAh g^{-1} (0.5 A g^{-})	[19]
Ca_2MnO_4	2 M $ZnSO_4$ + 0.1 M $MnSO_4$	0.8 -1.8V	100 mAh g^{-1} (1 A g^{-1})	[20]
VO_2 (B) nanofibers	3M $Zn(CF3SO_3)_2$	0.3-1.5V	220 mAh g^{-1} (10 A g^{-1})	[21]
VO_2 (B)/rGO	1M $ZnSO_4$	0.3-1.1V	320 mAh g^{-1} at (5A g^{-1})	[22]
RGO/VO_2	3M $Zn(CF_3SO_3)_2$	0.3-1.3V	180 mAh g^{-1} at (8.0 A g^{-})	[23]
VO_2 nanorods	1M $ZnSO_4$	0.2-1.3V	220 mAh g^{-1} (3.0 A g^{-})	[24]
nsutite-type VO_2	2M $ZnSO_4$	0.2-1.2V	178 mAh g^{-1} (3.0 A g^{-})	[25]
VO_2 (D) hollow nanospheres	3M $ZnSO_4$	0.2-1.5V	202 mAh g^{-1} (5.0 A g^{-})	[26]
Ni-doped VO_2	3M $Zn(CF_3SO_3)_2$	0.2-1.4V	182 mA h g^{-1} (5 Ag^{-1})	[27]
VO_2 (B) nanobelts	3M $Zn(CF_3SO_3)_2$	0.2-1.4V	200 mAh g^{-1} (5.0 A g^{-})	[28]
$VO_2 \cdot 0.2H_2O$ nanocuboids	2M $ZnSO_4$	0.4-1.1V	215 mA h g^{-1} (8 Ag^{-1})	[29]
VO_2 nanoplate	1M $ZnSO_4$	0.2-1.0V	136 $mAhg^{-1}$ (2A g^{-1})	[30]

Reference

[1] Y. Li, Z. Huang, P.K. Kalambate, Y. Zhong, Z. Huang, M. Xie, Y. Shen, Y. Huang, *Nano Energy,* 2019, **60,** 752-759.

[2] D. Kundu, B.D. Adams, V. Duffort, S.H. Vajargah, L.F. Nazar, *Nat. Energy,* 2016, **1,** 161119.

[3] K. Zhu, T. Wu, K. Huang, A*dv. Energy Mater.,* 2019, **9,**1901968.

[4] X. Wang, B. Xi, X. Ma, Z. Feng, Y. Jia, J. Feng, Y. Qian, S. Xiong, *Nano Lett.* 2020, **20,** 2899-2906.

[5] H. Geng, M. Cheng, B. Wang, Y. Yang, Y. Zhang, C.C. Li, *Adv. Funct. Mater.* 2019, **30,** 1907684.

[6] P. He, Y. Quan, X. Xu, M. Yan, W. Yang, Q. An, L. He, L. Mai, *Small,* 2017, **13,** 1702551.

[7] J. Shin, D.S. Choi, H.J. Lee, Y. Jung, J.W. Choi, H, *Adv. Energy Mater.,* 2019, **9,** 1900083.

[8] Z. Cao, H. Chu, H. Zhang, Y. Ge, R. Clemente, P. Dong, L. Wang, J. Shen, M. Ye, P.M. Ajayan, *J. Mater. Chem. A,* 2019, **7,** 25262-25267.

[9] T. Chen, X. Zhu , X. Chen, Q. Zhang, X. Pan, *J. power Sources,* 2020, **477**, 228652.

[10] H. Qin, Z. Yang, L. Chen, X. Chen, L. Wang, *J. Mater. Chem. A,* 2018, **6,** 23757-23765.

[11] L. Wang, Z. Wu, M. Jiang, J. Lu, Q. Huang, Y. Zhang, L. Fu, M. Wu, Y. Wu, *J. Mater. Chem. A,* 2020, **8,** 9313-9321.

[12] L. Ma, S. Chen, C. Long, X. Li, Y. Zhao, Z. Liu, Z. Huang, B. Dong, J.A. Zapien, C. Zhi, *Adv. Energy Mater.,* 2019,**9,** 1902446.

[13] W. Wang, V.S. Kale, Z. Cao, S. Kandambeth, W. Zhang, J. Ming, P.T. Parvatkar, E. Abou-Hamad, O. Shekhah, L. Cavallo, M. Eddaoudi, H.N. Alshareef, *ACS Energy Lett.,* 2020, **5,** 2256-2264.

[14] Y. Zhao, L. Ma, Y. Zhu, P. Qin, H. Li, F. Mo, D. Wang, G. Liang, Q. Yang, W. Liu, C. Zhi, *ACS Nano,* 2019,**13,** 7270-7280.

[15] L. Ma, S. Chen, H. Li, Z. Ruan, Z. Tang, Z. Liu, Z. Wang, Y. Huang, Z. Pei, J.A. Zapien, C. Zhi, *Energy Environ. Sci.,* 2018, **11,** 521-2530.

[16] Q. Tan, X. Li, B. Zhang, X. Chen, Y. Tian, H. Wan, L. Zhang, L. Miao, C. Wang, Y. Gan, J. Jiang, Y. Wang, H. Wang, *Adv. Energy Mater.,* 2020, **10**, 2001050.

[17] T. Xiong, Z.G. Yu, H. Wu, Y. Du, Q. Xie, J. Chen, Y.W. Zhang, S.J. Pennycook, W.S.V. Lee, J. Xue, *Adv. Energy Mater.,* 2019, **9**, 1803815.

[18] Y. Cai, R. Chua, S. Huang, H. Ren, M. Srinivasan, C*hem. Eng. J.,* 2020, **396**, 125211.

[19] W. Li, X. Gao, Z. Chen, R. Guo, G. Zou, H. Hou, W. Deng, X. Ji, J. Zhao, *Chem. Eng. J.,* 2020, **402**, 125509.

[20] S. Guo, S. Liang, B. Zhang, G. Fang, D. Ma, J. Zhou, *ACS Nano,* 2019, **13**, 13456-13464.

[21] W. Zhang, Y. Xiao, C. Zuo, W. Tang, G. Liu, S. Wang, W. Cai, S. Dong, P. Luo, *ChemSusChem* 2021, **14**, 971.

[22] F. Cui, J. Zhao, D. Zhang, Y. Fang, F. Hu, K. Zhu, *Chem. Eng J.,* 2020, **390**, 124128.

[23] X. Dai, F. Wan, L.L. Zhang, H.M. Cao, Z.Q. Niu, *Energy Storage Mater*., 2019, **17**, 143-150.

[24] L. Chen, Y. Ruan, G. Zhang, Q. Wei, Y. Jiang, T. Xiong, P. He, W. Yang, M. Yan, Q. An, L. Mai, *Chem. Mater.,* 2019, **31**, 699-706.

[25] Z. Cao, L. Wang, H. Zhang, X. Zhang, J. Liao, J. Dong, J. Shi, P. Zhuang, Y. Cao, M. Ye, J. Shen, P.M. Ajayan, *Adv. Funct. Mater.,* 2020, **30**, 202000472.

[26] L Chen, Z.H Yang, Y.G Huang, *Nanoscale*, 2019, **11**, 13032

[27] Y. Cai, R. Chua, Z. Kou, H. Ren, D. Yuan, S. Huang, S. Kumar, V. Verma, P. Amonpattaratkit, M. Srinivasan, *ACS Appl. Mater. Interfaces,* 2020, **12**, 36110-36118.

[28] K. Zhu, T. Wu, S. Sun, W. van den Bergh, M. Stefik, K. Huang, *Energy Storage Mater.,* 2020, **29**, 60-70.

[29] D. Jia, K. Zheng, M. Song, H. Tan, A. Zhang, L. Wang, L. Yue, D. Li, C. Li, J. Liu, *Nano Res.,* 2020, **13**, 215-224.

[30] Q, Pang, H. Zhao, R. Lian, Q. Fu, Y.Wei, Sarapulova, J. Sun, C. Wang, G. Chen, Ehrenberg, *J. Mater. Chem. A,* 2020, **8**, 9567-9578